

Breaking crosstalk limits to dynamic holography using orthogonality of high-dimensional random vectors

Ghaith Makey^{1,2}, Özgün Yavuz³, Denizhan K. Kesim³, Ahmet Turnalı³, Parviz Elahi^{1,2}, Serim Ilday¹, Onur Tokel^{1,2*} and F. Ömer Ilday^{1,2,3*}

Holography is the most promising route to true-to-life three-dimensional (3D) projections, but the incorporation of complex images with full depth control remains elusive. Digitally synthesized holograms¹⁻⁷, which do not require real objects to create a hologram, offer the possibility of dynamic projection of 3D video^{8,9}. Despite extensive efforts aimed at 3D holographic projection¹⁰⁻¹⁷, however, the available methods remain limited to creating images on a few planes¹⁰⁻¹², over a narrow depth of field^{13,14} or with low resolution¹⁵⁻¹⁷. Truly 3D holography also requires full depth control and dynamic projection capabilities, which are hampered by high crosstalk^{9,18}. The fundamental difficulty is in storing all the information necessary to depict a complex 3D image in the 2D form of a hologram without letting projections at different depths contaminate each other. Here, we solve this problem by pre-shaping the wavefronts to locally reduce Fresnel diffraction to Fourier holography, which allows the inclusion of random phase for each depth without altering the image projection at that particular depth, but eliminates crosstalk due to the near-orthogonality of large-dimensional random vectors. We demonstrate Fresnel holograms that form on-axis with full depth control without any crosstalk, producing large-volume, high-density, dynamic 3D projections with 1,000 image planes simultaneously, improving the state of the art^{12,17} for the number of simultaneously created planes by two orders of magnitude. Although our proof-of-principle experiments use spatial light modulators, our solution is applicable to all types of holographic media.

Holography was originally invented to bypass the limitations of lens aberrations to electron microscopy^{19,20}, but it was its optical implementation that captured the imagination of the general public as a means for true-to-life recreation of 3D objects^{21,22}. Interest in this hitherto elusive goal is rapidly intensifying with the advent of virtual and augmented reality^{23,24}. A hologram comprises a holographic field and a physical medium in which to store it. There is steady progress in improving the physical medium, using metamaterials²⁻⁴, graphene²⁵, photorefractives²⁶, stretchable materials¹² and silicon⁶, improving metrics such as viewing angle¹⁷, pixel size²⁵, spectral response²⁵ and reconfigurability¹², although deformable mirrors¹⁷ and spatial light modulators (SLMs)²² are still the most commonly used components. The key to creating realistic-looking projections, independent of the media, is the hologram field itself, which is often digitally synthesized. Computer-generated holograms (CGHs)¹⁻⁷ do

not require real objects to create the hologram, which is essential for dynamic holography²⁴. Both Fourier and Fresnel holography have been used to create CGHs. Fourier holograms based on established methods^{27,28} such as the kinoform technique²⁷ can project only around the focal plane of a lens, limiting them primarily to microscopy applications¹¹. In contrast, Fresnel holography can project arbitrarily large images with 3D depth²⁹. The first 3D Fresnel CGHs were based on the ping-pong algorithm¹⁰, which works only for two-plane projection. Alternative methods have been proposed³⁰, but they are computationally heavy, do not project deep 3D scenes and cannot be implemented on common holographic media. A popular approach is to use look-up tables^{15,22}, but this is limited to reconstructing simple, low-resolution images. Projection quality can be improved with cascaded diffractive elements³¹, which is a costly and overly complicated method. Although projections of up to several tens of planes have been demonstrated¹⁷, these were only for a single dot in each plane and could not be obtained simultaneously, but had to be created sequentially. For anything more complex than a single dot, earlier demonstrations have been limited to a few image planes, such the three letters shown in ref. ¹¹. In all of these approaches, simultaneous multiplane image projection remains extremely limited by high crosstalk, resulting in projections that are too flat, too blurry or too low resolution, and that can only be viewed from within a tiny angular range.

To approximate a genuinely 3D object, a large number of images must be projected to successive planes (Fig. 1a) and all these images must be embedded into the hologram. We use a succession of lenses, implemented as Fresnel zone plates (FZPs), to focus each image to a particular plane. The first key step is to shape the wavefronts to reduce the Fresnel diffraction to the Fourier transform locally at each image plane, so that construction of a single Fresnel hologram comprising an arbitrary number of planes is reduced to a trivial superposition operation (Fig. 1b). The second step is to add random phase at each image plane to suppress crosstalk: an image can be regarded as an N -dimensional vector, where N is the number of pixels (order of 10^6). Random vectors become asymptotically orthogonal in the limit of $N \rightarrow \infty$ (Fig. 1c). This property, which is due to the central limit theorem and the law of large numbers, leads to the elimination of any coherent trace of the images on each other during hologram reconstruction, virtually eliminating crosstalk from the reconstructed images (Fig. 1d).

We pre-shape the wavefront at each focus not only to allow for superposition of many holograms to form a single one, but also to

¹UNAM - National Nanotechnology Research Center and Institute of Materials Science and Nanotechnology, Bilkent University, Ankara, Turkey.

²Department of Physics, Bilkent University, Ankara, Turkey. ³Department of Electrical and Electronics Engineering, Bilkent University, Ankara, Turkey.

*e-mail: otokel@bilkent.edu.tr; ilday@bilkent.edu.tr

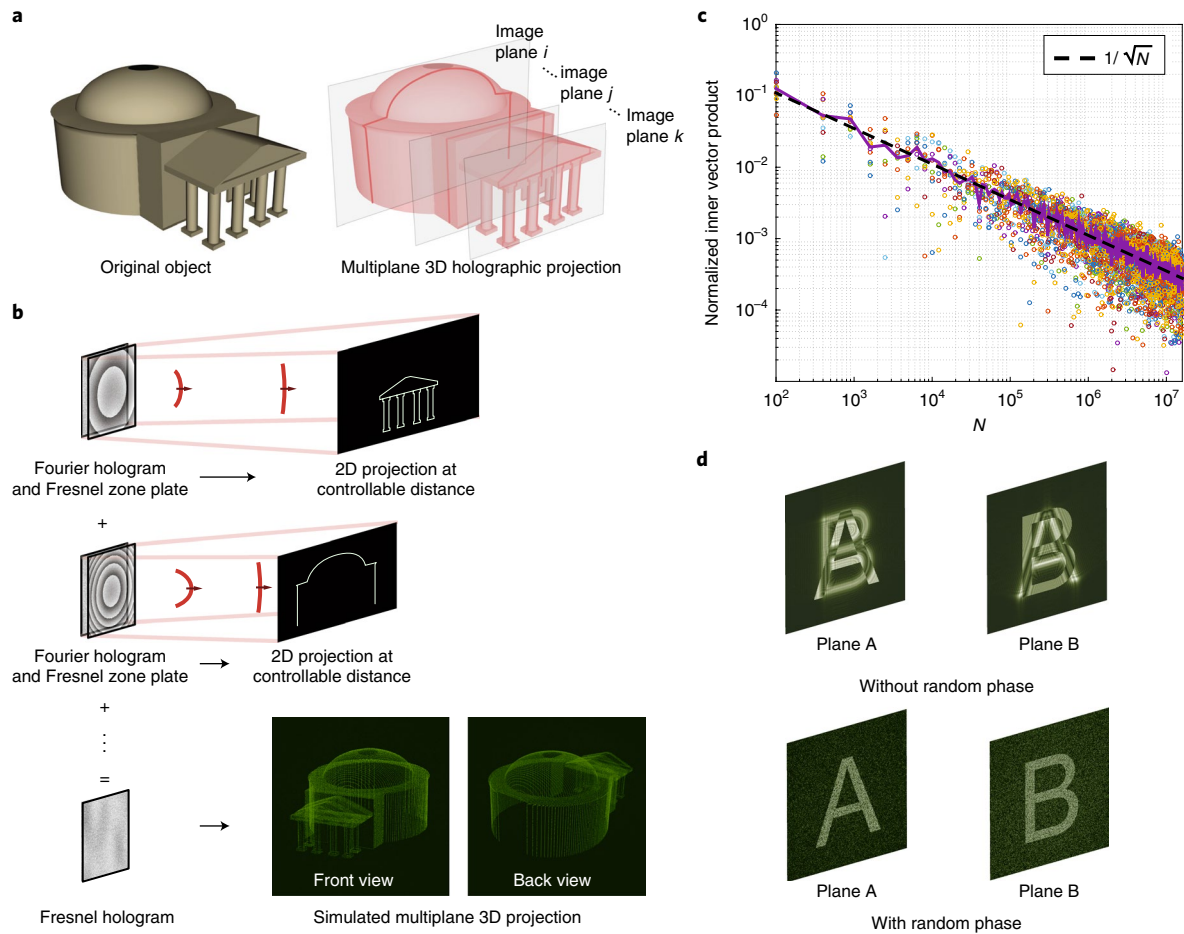


Fig. 1 | Principle of crosstalk suppression in multiplane projection. **a**, Computer-generated holograms need to comprise large numbers of individual holograms of 2D images projected to different foci to serve as realistic representations of 3D objects, thus requiring excellent depth control, separation and elimination of crosstalk. **b**, We simultaneously project multiplane images with controllable separation, while remaining in the Fresnel regime. To achieve this, we add a phase FZP to a phase Fourier hologram to shift its image to the focal plane of the FZP. This corresponds to projecting a Fourier image in the Fresnel regime. Multiple holograms can be generated in this way, each designed to project a slice of a 3D object, then superposed to create a single Fresnel hologram. **c**, Normalized inner product of two complementary chequerboard images, calculated as a function of total pixel size N . The phase of each source image is random, uniformly distributed over $0-2\pi$. **d**, Adding random phase to each image suppresses unwanted crosstalk.

prevent the random phase that we add from distorting the images to which they are added. This would be nearly automatic if the reconstructed image were to have a flat wavefront at its focal plane, as would be the case for Fourier holography, but Fourier holography is limited to the far field. Fresnel holograms can operate at virtually any distance but the propagation kernel is parabolic. We pre-shape the wavefront of the source hologram with a parabolic phase such that it becomes locally flat at each focus, much like the prechirping of an ultrashort laser pulse entering a dispersive medium, where it accumulates a parabolic phase shift, only to be chirp-free at a specific propagation distance. Consider a Fresnel hologram that projects a complex field distribution:

$$W(x, y, z) = \frac{e^{j\frac{2\pi z}{\lambda}}}{j\lambda z} e^{j\frac{\pi}{\lambda z}(x^2+y^2)} \iint_{-\infty}^{\infty} \left\{ H(\xi, \eta) e^{j\frac{\pi}{\lambda z}(\xi^2+\eta^2)} \right\} e^{-j\frac{2\pi}{\lambda z}(x\xi+y\eta)} d\xi d\eta \quad (1)$$

where z is the distance between the image and hologram, (x, y) and (ξ, η) are the spatial coordinates at the image and hologram planes, respectively, $H(\xi, \eta)$ is the complex field distribution of the hologram and λ is the wavelength¹. The main difference from a Fourier hologram is the presence of the term, $e^{j\frac{2\pi}{\lambda z}(x^2+y^2)}$. If this term can be

cancelled at a specific plane $z = z_0$, this would correspond to reducing the Fresnel diffraction to a Fourier transform at that plane. To this end, we construct the hologram, $H(\xi, \eta)$, in the form of $H(\xi, \eta) = F(\xi, \eta) e^{-j\frac{\pi}{\lambda z_0}(\xi^2+\eta^2)}$, where $F(\xi, \eta)$ is the Fourier hologram of the product of the desired image, $U(x, y)$, and a random phase, $e^{-j\phi(x,y)}$, which is added to suppress crosstalk (see Methods for details). The appended quadratic term counteracts the effect of the propagation kernel, such that, at the particular position of z_0 , the projected field is

$$W(x, y, z_0) = \frac{e^{j\frac{2\pi}{\lambda}z_0}}{j\lambda z_0} e^{j\frac{\pi}{\lambda z_0}(x^2+y^2)} \iint_{-\infty}^{\infty} F(\xi, \eta) e^{-j\frac{2\pi}{\lambda z_0}(x\xi+y\eta)} d\xi d\eta \quad (2)$$

which is similar, in form, to a Fourier hologram. For maximum generality and best results, $F(\xi, \eta)$ should be complex. However, we restrict ourselves to using phase-only holograms, so a single SLM is sufficient for experimental realization. The points with phase $n\pi$ for $e^{-j\frac{2\pi}{\lambda z_0}(\xi^2+\eta^2)}$ correspond to concentric circles with radii, $r_n = \sqrt{n\lambda z_0}$, which closely approximate a FZP of focal length f , for integer n . Direct superposition of a phase-type FZP on a phase-type Fourier hologram will generate a single-plane, phase-type Fresnel hologram, where the focal length of the FZP can be used to controllably

translate the image to any distance z beyond the Talbot length (Fig. 1b). Then, construction of a single Fresnel hologram with M multiplane projections is straightforward: $H_M(\xi, \eta) = \sum_{s=1}^M F_s(\xi, \eta) e^{-j\frac{\pi}{\lambda z_s}(\xi^2 + \eta^2)}$, where $F_s(\xi, \eta)$ are the Fourier holograms of the images to be projected at $z = z_s$. This way, the otherwise extremely complicated procedure of packing many images into a single Fresnel hologram becomes a trivial superposition operation. The final Fresnel hologram is

$$H_M(\xi, \eta) = \sum_{s=1}^M \left\{ \underbrace{-\frac{e^{-j\frac{2\pi}{\lambda} z_f}}{j\lambda z_f}}_{\text{Intended image}} \int \int_{-\infty}^{\infty} U_s(x, y) \underbrace{e^{-j\phi_s(x, y)}}_{\text{Random phase}} dx dy \right\} \underbrace{e^{j\frac{2\pi}{\lambda z_f}(x\xi + y\eta)}}_{\text{Fresnel zone plate}} \left\{ e^{-j\frac{\pi}{\lambda z_s}(\xi^2 + \eta^2)} \right\} \quad (3)$$

After lengthy, but straightforward calculations, the image projected by this hologram at each of the image planes reduces to

$$W'(x', y', z_i) = k \left(U_i'(x', y') e^{-j\phi_i'(x', y')} + \frac{j}{\pi} \sum_{\substack{s=1 \\ s \neq i}}^M Y_s(x', y') \right) \quad (4)$$

where k is a constant, $Y_s(x', y') \equiv U_s'(x', y') e^{j\phi_s'(x', y')} \otimes e^{j(x'^2 + y'^2)}$ (the sign \otimes denotes convolution) and x' and y' are normalized versions

of x and y . The primed terms, $U_i'(x', y')$, $\phi_i'(x', y')$ and $W'(x', y', z_i)$ are functions of the normalized coordinates, but remain otherwise identical in form and amplitude. The 3D image formed on any conventional detector is given by the light intensity, which is proportional to

$$\begin{aligned} |W'(x', y', z_i)|^2 &= |k|^2 \left(\underbrace{|U_i'(x', y')|^2}_{\text{Intended image}} + \frac{1}{\pi^2} \sum_{\substack{s=1 \\ s \neq i}}^M |Y_s(x', y')|^2 \right. \\ &+ \frac{j}{\pi} \sum_{\substack{s=1 \\ s \neq i}}^M (U_i'(x', y')^* e^{j\phi_i'(x', y')} Y_s(x', y')) \\ &- U_i'(x', y') e^{-j\phi_i'(x', y')} Y_s(x', y')^* \\ &+ \frac{1}{\pi^2} \sum_{\substack{s=1 \\ s > m}}^M \sum_{m=1}^M (Y_s(x', y')^* Y_m(x', y')) \\ &\left. + Y_s(x', y') Y_m(x', y')^* \right) \end{aligned} \quad (5)$$

Here, the first term, $|U_i'(x', y')|^2$, corresponds to perfect projection of the intended image. The second term is a sum of $M - 1$ individually as well as mutually random images due to the convolution of the random phases and parabolic wavefronts; in practice, they add white noise to the ideal image and with increasing M , their contribution, already suppressed by a factor of π^2 , regresses further to the mean by the central limit theorem. The third and fourth terms are sums over order of M and M^2 terms, respectively, and each is in a form such that their average contribution over the image is in a similar form to the orthogonality of two images. This contribution is ensured to be almost surely zero in the limit of $N \rightarrow \infty$ by the orthogonality of high-dimensional mutually random vectors. Furthermore, these terms are all mutually independent and of zero expected values, and their summations get closer to zero by the central limit theorem for large M . Overall, the final result for any image plane, i , is the ideal image, $|U_i(x, y)|^2$ and a small amount of white noise. Practically (in

all examples considered, N is in the range $10^5 - 10^7$), crosstalk is completely eliminated.

The algorithmic implementation of our method is shown in Fig. 2a. In step 1, we start with a stack of target images that form the desired 3D projection. Each image is passed through a pre-processing stage, where random phase is added. In step 2, each image goes through a number of iterations to generate its Fourier CGH (kinoform). We use an iterative Fourier transform algorithm (IFTA) to generate a set of kinoforms, $F_i(\xi, \eta)$, each to be used for projecting an image plane of the targeted 3D projection. We use the adaptive additive IFTA³², which is fast enough for real-time applications. In step 3, each Fourier CGH is superposed with a phase FZP, to shift its projection to the focal plane of the corresponding FZP. In step 4, the translated holograms are added in complex form to create a single complex Fresnel hologram. After the complex superposition, the phase of the resulting sum is used as the final hologram.

We first show a set of simulation results for the simultaneous projection of 1,000 images to their respective planes from a single $4,000 \times 4,000$ pixel 3D hologram. Light is able to focus/defocus repeatedly along the propagation axis to form high-fidelity images with minimal crosstalk (Fig. 2b and Supplementary Video 1). Next, as a demonstration of how the front, back and many in-between layers of a complex 3D object can be represented through simultaneous projection of multiple planes, we show a 3D spacecraft that can be viewed with the correct perspective from any direction over the full 4π solid angle (Fig. 2c and Supplementary Video 2). The simulation assumes a medium that emits or scatters light only at foci (for instance, ref. 33 or Supplementary Fig. 1). We also demonstrate the possibility of projecting much more complex images from a single Fresnel hologram (Fig. 2d and Supplementary Video 3). As expected, we find that larger hologram sizes in terms of geometry and pixel count lead to lower crosstalk between adjacent planes, increasing the number of separable planes. This increased axial resolution is enabled by FZPs, each acting like an imaging lens, extending over the entire hologram. Larger hologram sizes enable lenses with higher numerical aperture, leading to a smaller depth of field at each plane, which allows for projecting at a higher number of planes. The performance of 3D holograms in terms of the number of projected planes and image quality is further discussed in the Methods. Multiplane projection achieved with our method is applicable at any distance beyond the Talbot zone, and no physical lens is required to project the images. Thus, the method can be used to project over a large depth of field at nearly arbitrarily separated planes, for example to depict a closed-surface 3D object using a single hologram (Figs. 1b and 2c and Supplementary Video 2).

We performed a set of experiments to prove the concept using different laser wavelengths and SLMs (Fig. 3a; see Methods). The SLM used in the experiments limited the holograms to 512×512 pixels. We first demonstrate two-plane reconstruction from a single Fresnel hologram, projecting greyscale images that are high resolution in terms of the number of active (non-black) pixels (Fig. 3b). Next, we show a four-plane projection from a single Fresnel hologram (Fig. 3c). Finally, we demonstrate the ability to project images over a large number of planes (Fig. 3d). This projection, encompassing 11 images of on-axis letters, constitutes the highest number of planes experimentally imaged from a single Fresnel CGH. Altogether, these results highlight the exceptional flexibility achieved in the design of 3D Fresnel CGHs. A second group of experiments demonstrate the applicability of our method to low-cost 3D projection. We used a green laser and a liquid crystal on silicon (LCoS) SLM that we extracted from a very low-cost consumer-grade projector. The results of the 3D display prototype demonstrating large-volume projection are shown in Supplementary Fig. 1. The hologram was designed to project three back-to-back images at different depths. We also implemented a dynamic display by animating three videos

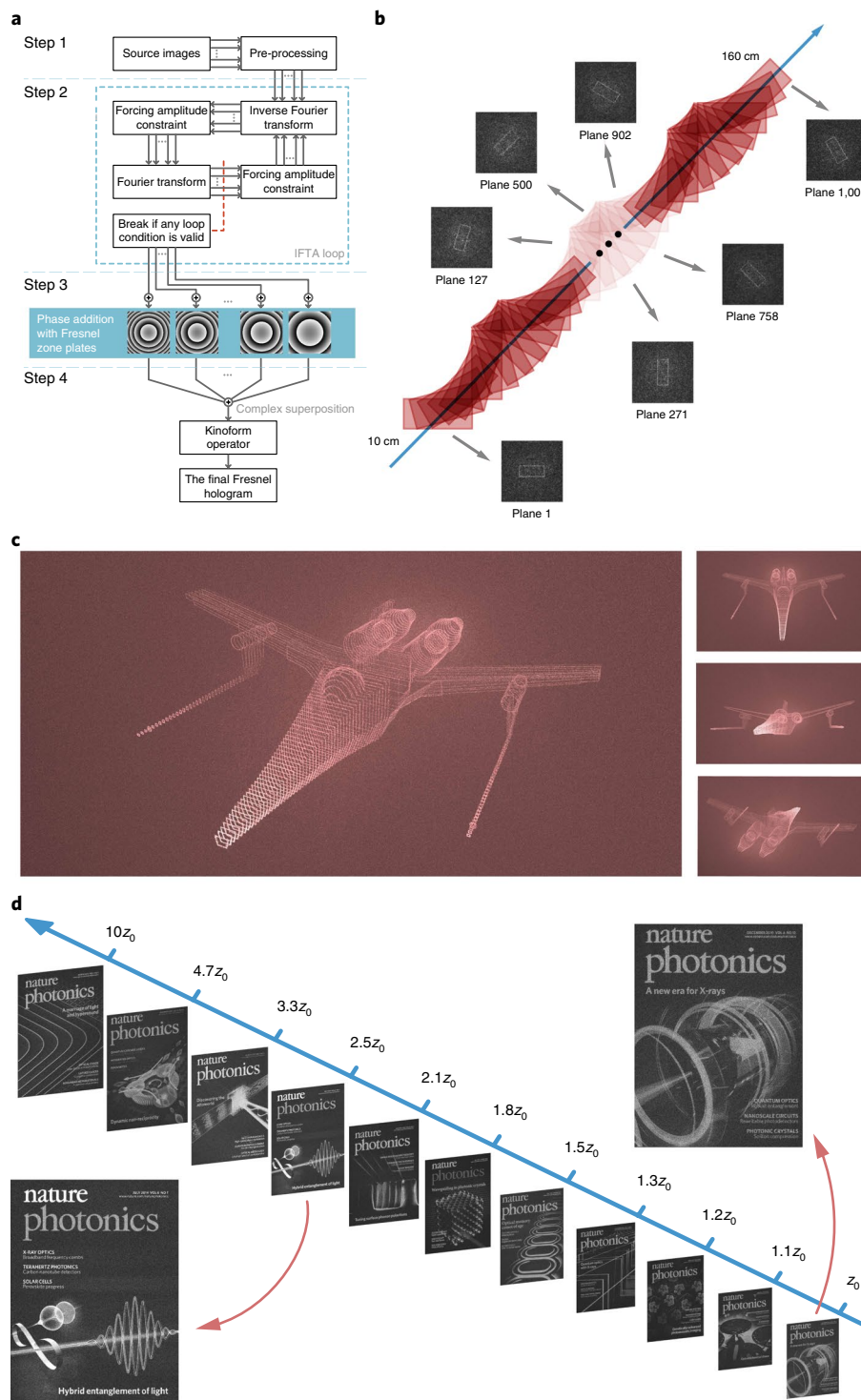


Fig. 2 | Algorithm and implementation of 3D Fresnel holograms. **a**, Outline of the 3D Fresnel algorithm. **b**, Representative schematic and simulations corresponding to a large-volume high-density 3D Fresnel hologram extending 150 cm in depth. The simultaneously projected 1,000 on-axis images are simulated using a $4,000 \times 4,000$ hologram. **c**, Simulation of a complex projected object from various angles. 100 planes are simultaneously projected from a single $4,000 \times 4,000$ pixel hologram to distances spanning 10–20 cm from the hologram. **d**, Simulation of 11 high-definition ($1,435 \times 1,080$ pixels) images projected simultaneously from a single 16,000 hologram. The projection extends over 90 cm. Panel **d** adapted from *Nature Photonics* covers, from left to right: Liesbet van Lanschoot, Raphaël van Laer and Amin Abbasi, Ghent University-IMEC; Erik Zumalt, Dimitrios Sounas and Andrea Alù, The University of Texas at Austin; Christian Hackenberger, Ludwig-Maximilians Universität; Marco Bellini (INO-CNR, Italy); Chul Soo Kim, Chase T. Ellis, Joseph G. Tischler, US Naval Research Laboratory; Joshua D. Caldwell, Vanderbilt University; Stephen Eisenmann (University of Illinois at Urbana-Champaign); Fengnian Xia et al.; DESY/Ralf Röhlsberger, Boris Kucicak; Paul Beard; F. Monifi, S. K. Özdemir, B. Peng and L. Yang; Richard B. Baxley and Tenio Popmintchev.

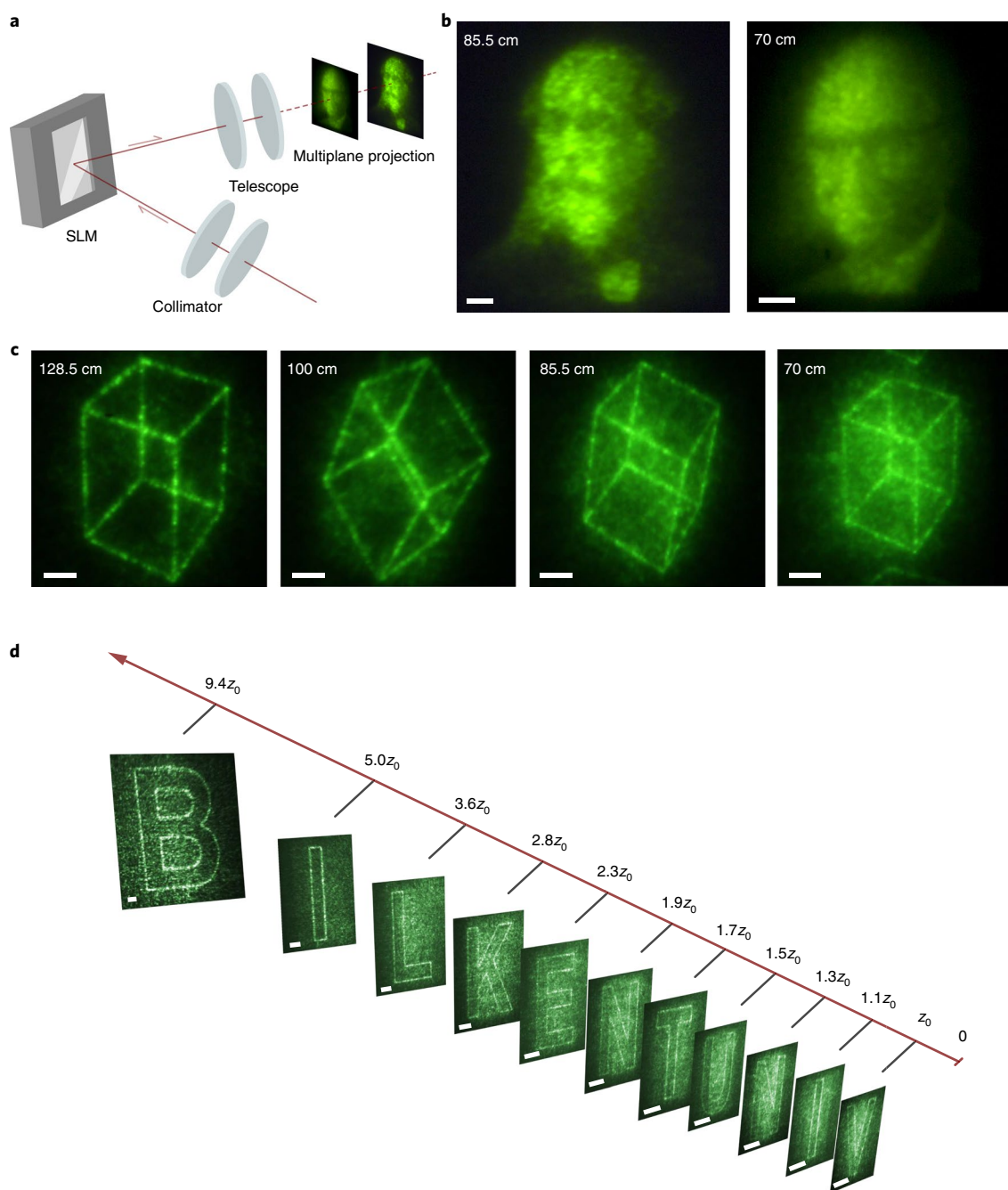


Fig. 3 | Experimental demonstration of multiplane projection. **a**, Optical set-up used in the experiments. **b**, Two-plane, high-resolution simultaneous projection (portraits of Maxwell and Gabor). The distances from the hologram are 85.5 and 70 cm. **c**, Four-plane simultaneous projection of a rotating cube. The distances from the hologram are 128.5, 100, 85.5 and 70 cm. **d**, Eleven-plane simultaneous projection of the letters spelling BILKENT UNIV, where $z_0 = 18$ cm. Scale bars, 2 mm. Each image set is projected without lateral shift from a single hologram. Panel **b** adapted from: left, <https://archive.org/details/popularsciencemo78newyuoft/page/518>; right, © National Portrait Gallery, London.

simultaneously, which were projected on-axis, without lateral shift (Supplementary Video 4).

The results reported here are far from the fundamental limits imposed by physical optics; the quality and number of image planes scale up linearly with the number of pixels available from the holographic media, accompanied by a merely linear increase in required computation time. These two favourable scaling properties are direct consequences of the elimination of crosstalk and our wavefront engineering trick that reduces Fresnel diffraction locally to Fourier transforms respectively. SLMs with much higher numbers of pixels than those we have used in our experiments have been available

since 2009³⁴, which suggests that more dramatic demonstrations are already possible. Our method can be used for real-time, video-rate dynamic holography, even with current computer technology (see Methods). Such real-time capability can conceivably be used to incorporate occlusion effects (see Supplementary Information). Although our proof-of-concept results are targeted at various 3D display applications, including volumetric displays³⁵, in diverse scenarios, such as medical visualization or air traffic control, our method can find use in a wide range of applications, including modern electrooptical devices³⁶, microscopy¹¹ and laser-material interactions. Just as holography was invented for electron microscopy,

but had an impact in optics, given the rich history of judicious use of random fields in optics³⁷ and the generality of the mathematical result that our approach is based on, there may be exciting applications in near-zero epsilon optics³⁸ and imaging with flat optics².

Online content

Any methods, additional references, Nature Research reporting summaries, source data, statements of data availability and associated accession codes are available at <https://doi.org/10.1038/s41566-019-0393-7>.

Received: 28 October 2018; Accepted: 15 February 2019;

Published online: 22 March 2019

References

- Goodman, J. W. *Introduction to Fourier Optics* (Roberts & Company, 2005).
- Yu, N. & Capasso, F. Flat optics with designer metasurfaces. *Nat. Mater.* **13**, 139–150 (2014).
- Arbabi, A., Horie, Y., Bagheri, M. & Faraon, A. Dielectric metasurfaces for complete control of phase and polarization with subwavelength spatial resolution and high transmission. *Nat. Nanotechnol.* **10**, 937–943 (2015).
- Zheng, G. X. et al. Metasurface holograms reaching 80% efficiency. *Nat. Nanotechnol.* **10**, 308–312 (2015).
- Li, L. et al. Electromagnetic reprogrammable coding-metasurface holograms. *Nat. Commun.* **8**, 197 (2017).
- Tokel, O. et al. In-chip microstructures and photonic devices fabricated by nonlinear laser lithography deep inside silicon. *Nat. Photon.* **11**, 639–645 (2017).
- Melde, K., Mark, A. G., Qui, T. & Fisher, P. Holograms for acoustics. *Nature* **537**, 518–522 (2016).
- Smalley, D. E., Smithwick, Q. Y. J., Bove, V. M., Barabas, J. & Jolly, S. Anisotropic leaky-mode modulator for holographic video displays. *Nature* **498**, 313–317 (2013).
- Sugie, T. et al. High-performance parallel computing for next-generation holographic imaging. *Nat. Electron.* **1**, 254–259 (2018).
- Dorsch, R. G., Lohmann, A. W. & Sinzinger, S. Fresnel ping-pong algorithm for two-plane computer-generated hologram display. *Appl. Opt.* **33**, 869–875 (1994).
- Hernandez, O. et al. Three-dimensional spatiotemporal focusing of holographic patterns. *Nat. Commun.* **7**, 11928 (2016).
- Malek, S. C., Ee, H.-S. & Agarwal, R. Strain multiplexed metasurface holograms on a stretchable substrate. *Nano Lett.* **17**, 3641–3645 (2017).
- Wakunami, K. et al. Projection-type see-through holographic three-dimensional display. *Nat. Commun.* **7**, 12954 (2016).
- Almeida, E., Bitton, O. & Prior, Y. Nonlinear metamaterials for holography. *Nat. Commun.* **7**, 12533 (2016).
- Kim, S.-C. & Kim, E.-S. Fast computation of hologram patterns of a 3D object using run-length encoding and novel look-up table methods. *Appl. Opt.* **48**, 1030–1041 (2009).
- Huang, L. Three-dimensional optical holography using a plasmonic metasurface. *Nat. Commun.* **4**, 2808 (2013).
- Yu, H., Lee, K., Park, J. & Park, Y. Ultrahigh-definition dynamic 3D holographic display by active control of volume speckle fields. *Nat. Photon.* **11**, 186–192 (2017).
- Li, X. et al. Multicolor 3D meta-holography by broadband plasmonic modulation. *Sci. Adv.* **2**, e1601102 (2016).
- Gabor, D. A new microscopic principle. *Nature* **161**, 777–718 (1948).
- Gabor, D., Kock, W. E. & Stroke, G. W. Holography. *Science* **173**, 11–23 (1971).
- Yaras, F., Kang, H. & Onural, L. State of the art in holographic displays: a survey. *J. Disp. Tech.* **6**, 443–454 (2010).
- Tsang, P. W. M. & Poon, T. C. Review on the state-of-the-art technologies for acquisition and display of digital holograms. *IEEE Trans. Industr. Inform.* **12**, 886–901 (2016).
- Khorasaninejad, M., Ambrosio, A., Kanhaiya, P. & Capasso, F. Broadband and chiral binary dielectric meta-holograms. *Sci. Adv.* **2**, e1501258 (2016).
- Maimone, A., Georgiou, A. & Kollin, J. S. Holographic near-eye displays for virtual and augmented reality. *ACM Trans. Graph.* **36**, 85 (2017).
- Li, X. P. et al. Athermally photoreduced graphene oxides for three-dimensional holographic images. *Nat. Commun.* **6**, 6984 (2015).
- Blanche, P. A. et al. Holographic three-dimensional telepresence using large-area photorefractive polymer. *Nature* **468**, 80–83 (2010).
- Lesem, L. B., Hirsch, P. M. & Jordan, J. A. The kinoform: a new wavefront reconstruction device. *IBM J. Res. Dev.* **13**, 150–155 (1969).
- Makey, G., El-Daher, M. S. & Al-Shufi, K. Utilization of a liquid crystal spatial light modulator in a gray scale detour phase method for Fourier holograms. *Appl. Opt.* **51**, 7877–7882 (2012).
- Benton, S. A. & Bove, V. M. *Holographic Imaging* (Wiley-Interscience, 2008).
- Jackin, B. J. & Yatagai, T. 360 degrees reconstruction of a 3D object using cylindrical computer generated holography. *Appl. Opt.* **50**, H147–H152 (2011).
- Gülse, A. A. & Jenkins, B. K. Cascaded diffractive optical elements for improved multiplane image reconstruction. *Appl. Opt.* **52**, 3608–3616 (2013).
- Dufresne, E., Spalding, G., Dearing, M., Sheets, S. & Grier, D. Computer generated holographic optical tweezer arrays. *Rev. Sci. Instrum.* **72**, 1810–1816 (2001).
- Hsu, C. W. et al. Transparent displays enabled by resonant nanoparticle scattering. *Nat. Commun.* **5**, 3152 (2014).
- Furuya, M., Sterling, R., Bleha, W. & Inoue, Y. D-ILA full resolution 8K projector. In *SMPTE Annu. Tech. Conf. Expo* (SMPTE, 2009).
- Smalley, D. E. et al. A photophoretic-trap volumetric display. *Nature* **553**, 486–490 (2018).
- Yue, Z., Xue, G., Liu, J., Wang, Y. & Gu, M. Nanometric holograms based on a topological insulator material. *Nat. Commun.* **8**, 15354 (2017).
- Segev, M., Silberberg, Y. & Christodoulides, D. N. Anderson localization of light. *Nat. Photon.* **7**, 197–204 (2013).
- Engheta, N. Pursuing near-zero response. *Science* **340**, 286–287 (2013).

Acknowledgements

This work was supported partially by the European Research Council (ERC) Consolidator Grant ERC-617521 NLL, TÜBITAK under project 117E823 and the BAGEP Award of the Science Academy. The authors thank J. Toumi and M.S. El-Daher for discussions, L. Onural for critical reading of the manuscript and M. Yaman for inspiration.

Author contributions

G.M., O.T. and F.Ö.I. designed the research and interpreted the results with help from S.I. and Ö.Y. Experiments and simulations were performed by G.M., D.K.K., Ö.Y., A.T., O.T. and P.E.

Competing interests

The authors declare no competing interests.

Additional information

Supplementary information is available for this paper at <https://doi.org/10.1038/s41566-019-0393-7>.

Reprints and permissions information is available at www.nature.com/reprints.

Correspondence and requests for materials should be addressed to O.T. or F.Ö.I.

Publisher's note: Springer Nature remains neutral with regard to jurisdictional claims in published maps and institutional affiliations.

© The Author(s), under exclusive licence to Springer Nature Limited 2019

Methods

Experimental set-up. The experimental set-up (Fig. 3a), in the case of infrared illumination, includes a laser source (Yb-fibre laser operating at 1,035 nm, 300 mW), a collimator to nullify the divergence of the laser beam and enlarge the beam spot size to completely fill the hologram displayed on the SLM (~1 cm diameter), a reflective liquid-crystal-on-silicon SLM (Hamamatsu, X10468-03) with 800 × 600 pixels and 20 μm pixel size, and a digital camera (Canon, 60D). The SLM reflects the collimated, linearly polarized laser beam after modulating it with the Fresnel CGH. The beam is then optionally (used only in Fig. 3b,c) expanded with a ×3 telescope to block the zero-order diffraction, and then impinges on a screen. The hologram size is chosen to be 512 × 512 pixels, and the phase quantization is set to 202 levels. For visible illumination (Supplementary Fig. 1 and Supplementary Video 4) the set-up remains the same except for two changes. First, the wavelength of the laser is converted to green (517 nm) with second-harmonic generation in a beta barium borate (BBO) crystal. Second, the SLM is replaced with a visible one taken from a very inexpensive LCoS projector (LG, PH150G). A ×3 telescope is used (Supplementary Fig. 1 and Supplementary Video 4). The distances at which images can be projected and their sizes depend on the SLM size and its pixel dimensions, both of which can be scaled up with larger SLMs and smaller pixels, respectively.

Simulations of 3D Fresnel holograms. Simulations of the Fresnel hologram are carried out with the Fresnel diffraction equation. To achieve clear images, the zero order was filtered with a simulated 4f lens system. This corresponds to masking a small central section of the image spectrum, and then calculating the final image with the inverse Fourier transform of the spectrum.

Performance characterization of 3D Fresnel holograms. The performance of 3D Fresnel CGHs depends on the pixel size and pixel density of the hologram, the modulation type, the illumination wavelength and the amplitude and phase distributions at all image planes. In addition, practical limitations can affect the performance, such as experimental limitations in forming images in the vicinity of a reflection-type hologram. Therefore, finding an exact analytical expression involving all relevant parameters would be extremely complicated. Instead, we choose two metrics, which we believe still provide a good insight into the performance of 3D Fresnel holograms. The first is the root-mean-square error (r.m.s.e.) and the second is the depth of field (DoF). The former is based on image quality and is a measure of the similarity between the source images and projected images at each plane. The latter is based on the axial resolution and is related to the maximum number of separable planes for a given image quality.

The r.m.s.e. is first calculated for each image at its corresponding plane, and the results from all planes are then averaged to provide a collective quality metric for a 3D hologram. This value is used to evaluate how the projection quality changes as a function of the number of separate planes. For instance, the r.m.s.e. of a set of rotating back-to-back cubes is shown in Supplementary Fig. 2, showing that the error rises linearly with increasing projection planes. For a given error tolerance expressed in r.m.s.e., the number of image planes can be truncated.

In parallel, the DoF is used to evaluate the axial resolution. DoF is a metric used widely in photography in identifying the maximum distance between two separated objects at which the objects still appear acceptably sharp. Thus, crosstalk between images can be evaluated with DoF, at each plane (Supplementary Fig. 3). Minimizing crosstalk in multiplane projection is critical, because an image suffering significant crosstalk from neighbouring planes cannot accurately perform as a slice of a 3D projection.

We derive a DoF equation using two expressions, one for the Rayleigh range of a FZP and the other for spatial relationships between the sizes of the hologram and its image. We arrive at the following expression for the DoF at plane i , DoF _{i} (Supplementary Fig. 3):

$$\text{DoF}_i \propto \lambda \left[\frac{1}{n_h} \frac{z_i}{d\xi} \right]^2$$

where z_i is the focal length for image plane i , λ is the illuminating wavelength, $d\xi$ is the pixel size of the hologram and $n_h \times n_h$ is the resolution of Fresnel hologram. This expression provides a reasonably accurate estimation of the effect of the parameters included in it. For instance, for two similar three-plane projections, each with a different focal distance for the central plane, we would expect that the crosstalk suffered by the side images should be similar, given that the ratio of consecutive image separations is equal to the square of the ratio of central image locations. Supplementary Fig. 4 shows a simulation confirming this estimate.

We further see that increasing the hologram size ($n_h \times n_h$) would enable projecting to a higher number of image planes. This can also be understood from the following perspective: a FZP acts like a lens, so larger FZP sizes allow larger numerical apertures (NAs). A larger NA leads to tighter focus and, similar to the case in optical lenses, we expect the DoF for each projection plane to be reduced. In parallel, one expects reduced crosstalk, because the images defocus faster when removed from the focal plane of FZPs. Thus the axial resolution (that is, the number of separable planes) can be increased simply by increasing the hologram pixel

number. We note that one should not confuse the DoF of a slice of the 3D projection, discussed above in analogy to photography, with the DoF of the entire projection. The latter is meant to describe the depth of the entire 3D projection. In this sense, it is analogous to the DoF term described for the holovideo camera in ref. 29.

Holograms used in the experiments were of 512 × 512 pixels. If a higher-resolution SLM was available, for instance, an 8K SLM over which 4,000 × 4,000 pixel holograms are usable, then we expect the DoF values to be reduced by a factor of 60. This would allow significantly higher axial resolutions and many more image layers. We demonstrate this prediction by propagating such a high-resolution 3D Fresnel hologram (4,000 × 4,000 pixels) using the Fresnel equation. The simulation results shown in Supplementary Fig. 5 show the odd-numbered images from among the 200 images that are projected directly back to back using a single 3D Fresnel CGH.

The 3D projections in simulations are in good agreement with the experimental results. For instance, a set of representative simulations are compared with experiments in Supplementary Fig. 6. Simulations of a single 3D hologram that projects two high-resolution portraits to directly back-to-back planes are provided in Supplementary Fig. 6a. In comparison, the corresponding experiments shown in Supplementary Fig. 6b are in good agreement with the simulations. The hologram is 512 × 512 pixels and uses 20 μm pixels in both experiments and simulations.

Scaling of the number of planes with number of SLM pixels. We observed a linear scaling between the number of planes and number of pixels of the SLM. To see this, we assumed a distance between consecutive images as $z_{i+1} = z_i + \gamma(\text{DoF}_i + \text{DoF}_{i+1})$, where γ is an empirical parameter chosen to minimize crosstalk. This recursive relation can be directly used to calculate the image positions. The number of projected planes for given constants γ , z_i and $d\xi$ is calculated, resulting in linear scaling of the maximum number of planes with the total number of pixels (Supplementary Fig. 7), preserving the image quality (r.m.s.e. ≈ 0.24).

Computation time and possibility of real-time calculations for video-rate holography. The most time-consuming step in our calculations is the Fourier transform, which is well optimized for parallel computation, including for graphics processor unit (GPU) based computation. Furthermore, for video-rate holographic projections, it will rarely be the case that every part of the holographic image will change from one frame to the next. Much more commonly, changes will be limited to parts of the hologram. In that case, thanks to its superposition-based multiplane construction, large parts of our calculation would remain unchanged and would not need to be recalculated. For instance, if the canopy of the spacecraft in Fig. 2c opens up but the rest of the craft remains unchanged, only parts of the hologram describing the canopy will have to be recalculated. This unique property of our algorithm is similar to a technique commonly used in most compression algorithms and further eases the requirements on real-time calculations. The typical calculation time for the experimentally demonstrated 3D holograms presented here is about 22 s using a single-CPU computer (Intel Core i7 4790K). A speed-up of 275-fold is achieved using a modern GPU, resulting in an 80 ms calculation time for experimental projection (Nvidia GeForce GTX980). We note that already available advanced GPUs, such as the Nvidia Tesla v100, will allow another tenfold speed-up. Furthermore, these calculations were performed using Matlab for its convenience. Implementation of our algorithm in a low-level programming language, such as C, would probably result in at least a twofold improvement. The projected calculation time with these improvements is likely to allow video rates of 20 Hz. More specialized hardware, such as a field-programmable gate-array platform, can improve calculation times further. Given the past rate of development of computational hardware, calculation time and cost appear unlikely to pose a limitation to the real-time generation of 3D dynamic holograms at video rates using our approach.

Orthogonality of large random vectors. The orthogonality of large random vectors can be proved through several different approaches, including waist concentration theory³⁹. Here, we follow a simple approach based on the law of large numbers⁴⁰ and the central limit theorem.

Assume X and Y to be non-equal large uniformly random vectors of equal size N , which is large. After normalization the vectors become $X/\|X\|$ and $Y/\|Y\|$, where $\|X\|$ and $\|Y\|$ are the lengths of X and Y , respectively. The inner vector product of the two vectors is given as

$$\text{IP} = \frac{\langle X, Y \rangle}{\|X\| \cdot \|Y\|}$$

By the law of large numbers, $\|X\|/\sqrt{N} \rightarrow 1$ and $\|Y\|/\sqrt{N} \rightarrow 1$ with high probability for large N . Large N also yields $\langle X, Y \rangle/\sqrt{N} \rightarrow 1$ according to the central limit theorem. The inner product scales with $1/\sqrt{N}$, showing that large random vectors rapidly converge to zero, rendering these vectors orthogonal. Similarly, in multi-plane Fresnel holography, we see that adding random phase to source images renders them orthogonal and reduces the crosstalk between their corresponding projected images (Supplementary Fig. 8).

Orthogonality of two images. We begin by cautioning the reader that use of a single quantity to characterize the cumulative amount of crosstalk between two images, each comprising large numbers of elements, would, inevitably, prove insufficient for the most general use. Nevertheless, orthogonality, defined through the inner product, works as an excellent measure for a wide range of images, from simple, complementary geometric patterns to human portraits (Supplementary Fig. 8). We calculate this quantity as follows. The images, together with their phase, are represented in complex form and are treated as vectors. The baseline of each vector is corrected by its average value, and each is normalized by its length. We then simply calculate the inner product as

$$IP = \frac{|x_1 e^{j\alpha_1} y_1 e^{-j\beta_1} + x_2 e^{j\alpha_2} y_2 e^{-j\beta_2} + \dots + x_N e^{j\alpha_N} y_N e^{-j\beta_N}|}{\|X\| \|Y\|}$$

where the vectors are $X = (x_1 e^{j\alpha_1}, x_2 e^{j\alpha_2}, \dots, x_N e^{j\alpha_N})$ and $Y = (y_1 e^{j\beta_1}, y_2 e^{j\beta_2}, \dots, y_N e^{j\beta_N})$. N is the total number of pixels in each image.

Theoretical calculations. The first step is to configure the hologram to produce a flat 'propagation kernel' even though we are in the Fresnel regime, such that the projected field magnitude will correspond to the desired 2D image at a given z . This opens the door to adding a pure phase term to each plane in a way that does not alter the image formed at that plane. This is possible because an image will be formed by detecting the light intensity, which is proportional to the absolute square of the field, an operation that drops any pure phase contributions. If the projection $W(x, y, z)$ is of the form $W(x, y, z) = W_A(x, y, z) e^{j\phi(x, y, z)}$, then the image formed will be proportional to $|W_A(x, y, z)|^2$.

We start by recalling the Fresnel and Fourier hologram equations¹. We consider the Fourier hologram, $F(\xi, \eta)$, of an image $U(x, y)$, which is additionally multiplied by a random phase, $e^{-j\phi(x, y)}$, to suppress crosstalk, as will be shown below. The physical significance of being in the Fourier (Fraunhofer) regime is that $U(x, y) e^{-j\phi(x, y)}$ is the field that would be formed in the far field, at the plane $z = z_f$:

$$F(\xi, \eta) = -\frac{e^{-j\frac{2\pi}{\lambda} z_f}}{j\lambda z_f} \iint_{-\infty}^{\infty} U(x, y) e^{-j\phi(x, y)} e^{j\frac{2\pi}{\lambda z_f} (x\xi + y\eta)} dx dy \quad (6)$$

Here, $z_f \gg \pi(\xi^2 + \eta^2)/\lambda$, which is the Fraunhofer condition. Similarly, the image formed by such a Fourier hologram in the far field is given by

$$U(x, y) e^{-j\phi(x, y)} = \frac{e^{j\frac{2\pi}{\lambda} z_f}}{j\lambda z_f} \iint_{-\infty}^{\infty} F(\xi, \eta) e^{-j\frac{2\pi}{\lambda z_f} (x\xi + y\eta)} d\xi d\eta \quad (7)$$

The Fresnel hologram is more flexible in that it can project an image, $W(x, y, z_i)$, at some arbitrary plane, $z_i = z_0$, and is given by

$$H_0(\xi, \eta) = -\frac{e^{-j\frac{2\pi}{\lambda} z_0}}{j\lambda z_0} e^{-j\frac{\pi}{\lambda z_0} (\xi^2 + \eta^2)} \iint_{-\infty}^{\infty} W(x, y, z_0) e^{-j\frac{\pi}{\lambda z_0} (x^2 + y^2)} e^{j\frac{2\pi}{\lambda z_0} (x\xi + y\eta)} dx dy \quad (8)$$

Similarly, the image to be projected at a plane $z_i = z_0$, $W(x, y, z_0)$, by a Fresnel hologram, $H(\xi, \eta)$, is given by

$$W(x, y, z_0) = \frac{e^{j\frac{2\pi}{\lambda} z_0}}{j\lambda z_0} e^{j\frac{\pi}{\lambda z_0} (x^2 + y^2)} \iint_{-\infty}^{\infty} H(\xi, \eta) e^{j\frac{\pi}{\lambda z_0} (\xi^2 + \eta^2)} e^{-j\frac{2\pi}{\lambda z_0} (x\xi + y\eta)} d\xi d\eta \quad (9)$$

The main difference of the Fresnel hologram (equation (8)) from a Fourier hologram (equation (6)) is the presence of a parabolic wavefront, which can be cancelled, albeit only for a specific plane, if we construct the hologram in the form

$$H(\xi, \eta) = F(\xi, \eta) e^{-j\frac{\pi}{\lambda z_0} (\xi^2 + \eta^2)} \quad (10)$$

which projects an image, $W(x, y, z_i)$, at a plane $z_i = z_0$. As explained in the main text, with this arrangement, a simple superposition operation is sufficient to construct a multiplane Fresnel hologram that projects a different image to each plane:

$$H_M(\xi, \eta) = \sum_{s=1}^M F_s(\xi, \eta) e^{-j\frac{\pi}{\lambda z_s} (\xi^2 + \eta^2)} \quad (11)$$

Here, M is the total number of image planes, $F_s(\xi, \eta)$ is the Fourier hologram of the image to be projected to a plane at $z = z_s$. The final Fresnel hologram is

$$H_M(\xi, \eta) = -\sum_{s=1}^M \left[\frac{e^{-j\frac{2\pi}{\lambda} z_f}}{j\lambda z_f} \iint_{-\infty}^{\infty} \frac{U_s(x, y)}{\text{Intended image}} \frac{e^{-j\phi_s(x, y)}}{\text{Random phase}} \right. \\ \left. e^{j\frac{2\pi}{\lambda z_f} (x\xi + y\eta)} \right] e^{-j\frac{\pi}{\lambda z_s} (\xi^2 + \eta^2)} \quad (12)$$

Fresnel zone plate

We emphasize that the random phase, $e^{-j\phi_s(x, y)}$, is different and mutually independent for each plane, s . Next, we want to calculate the image projected by this hologram at an arbitrary plane i , and demonstrate how the addition of the random phase does not distort the image it is added to, but that the random phase added to the other images suppresses their crosstalk.

The image formed by this hologram at an arbitrary plane, z_i , is given by

$$W(x, y, z_i) = \frac{e^{j\frac{2\pi}{\lambda} z_i}}{j\lambda z_i} e^{j\frac{\pi}{\lambda z_i} (x^2 + y^2)} \iint_{-\infty}^{\infty} H_M(\xi, \eta) e^{j\frac{\pi}{\lambda z_i} (\xi^2 + \eta^2)} e^{-j\frac{2\pi}{\lambda z_i} (x\xi + y\eta)} d\xi d\eta \quad (13)$$

or using equation (11):

$$W(x, y, z_i) = \frac{e^{j\frac{2\pi}{\lambda} z_i}}{j\lambda z_i} e^{j\frac{\pi}{\lambda z_i} (x^2 + y^2)} \iint_{-\infty}^{\infty} \sum_{s=1}^M F_s(\xi, \eta) e^{-j\frac{\pi}{\lambda z_s} (\xi^2 + \eta^2)} e^{j\frac{\pi}{\lambda z_i} (\xi^2 + \eta^2)} \\ e^{-j\frac{2\pi}{\lambda z_i} (x\xi + y\eta)} d\xi d\eta \quad (14)$$

We now separate the sum into terms $s = i$ and $s \neq i$, and evaluating $e^{j\frac{\pi(z_s - z_i)}{\lambda z_s z_i} (\xi^2 + \eta^2)}$ in the limit of $z_s \rightarrow z_i$:

$$W(x, y, z_i) = \frac{e^{j\frac{2\pi}{\lambda} z_i}}{j\lambda z_i} e^{j\frac{\pi}{\lambda z_i} (x^2 + y^2)} \iint_{-\infty}^{\infty} F_i(\xi, \eta) e^{-j\frac{2\pi}{\lambda z_i} (x\xi + y\eta)} d\xi d\eta \\ + \frac{e^{j\frac{2\pi}{\lambda} z_i}}{j\lambda z_i} e^{j\frac{\pi}{\lambda z_i} (x^2 + y^2)} \iint_{-\infty}^{\infty} \sum_{\substack{s=1 \\ s \neq i}}^M F_s(\xi, \eta) e^{j\frac{\pi(z_s - z_i)}{\lambda z_s z_i} (\xi^2 + \eta^2)} e^{-j\frac{2\pi}{\lambda z_i} (x\xi + y\eta)} d\xi d\eta \quad (15)$$

Using the relation $\iint_{-\infty}^{\infty} F_i(\xi, \eta) e^{-j\frac{2\pi}{\lambda z_i} (x\xi + y\eta)} d\xi d\eta = j\lambda z_i e^{-j\frac{2\pi}{\lambda} z_i} U_i(x, y) e^{-j\phi_i(x, y)}$ (from equation (6)) to simplify the first term, interchanging the order of the summation and the integral transform for the second term, and making the transformations $f_x = \frac{\xi}{\lambda z_f}$ and $f_y = \frac{\eta}{\lambda z_f}$ to cast the integral transform into an inverse Fourier transform (see ref.¹), we obtain

$$W(x, y, z_i) = \frac{z_f}{z_i} e^{j\frac{2\pi}{\lambda} (z_i - z_f)} e^{j\frac{\pi}{\lambda z_i} (x^2 + y^2)} U_i(x, y) e^{-j\phi_i(x, y)} \\ + \frac{\lambda z_f^2}{j z_i} e^{j\frac{2\pi}{\lambda} z_i} e^{j\frac{\pi}{\lambda z_i} (x^2 + y^2)} \sum_{\substack{s=1 \\ s \neq i}}^M \iint_{-\infty}^{\infty} F_s(\lambda z_f f_x, \lambda z_f f_y) \\ e^{j\frac{\pi \lambda z_f^2}{z_s z_i} (z_s - z_i) (f_x^2 + f_y^2)} e^{-j2\pi (x f_x + y f_y)} df_x df_y \quad (16)$$

Now, let us use the following relations, where \mathcal{F} denotes Fourier transform:

$$F_s(\lambda z_f f_x, \lambda z_f f_y) = \frac{-e^{-j\frac{2\pi}{\lambda} z_f}}{j\lambda z_f} \iint_{-\infty}^{\infty} U(x, y) \\ e^{-j\phi(x, y)} e^{j2\pi (x f_x + y f_y)} dx dy \quad (17) \\ = \frac{-e^{-j\frac{2\pi}{\lambda} z_f}}{j\lambda z_f} \mathcal{F}\{U_s(x, y) e^{-j\phi_s(x, y)}\}$$

which is obtained by applying the same transformation above on equation (6) and using

$$e^{j\frac{\pi \lambda z_f^2}{z_s z_i} (z_s - z_i) (f_x^2 + f_y^2)} = -\frac{j z_f z_s}{\lambda z_f^2 |z_s - z_i|} \mathcal{F} \left\{ e^{-j\frac{\pi z_f z_s}{\lambda z_f^2} \frac{(x^2 + y^2)}{z_s - z_i}} \right\} \quad (18)$$

we rewrite the terms above as Fourier transforms themselves.

$$W(x, y, z_i) = \frac{z_f}{z_i} e^{j\frac{2\pi}{\lambda}(z_i-z_f)} e^{j\frac{\pi}{\lambda z_i}(x^2+y^2)} U_f(x, y) e^{-j\phi_f(x, y)} + \frac{\lambda z_f^2}{j z_i} e^{j\frac{2\pi}{\lambda} z_i} e^{j\frac{\pi}{\lambda z_i}(x^2+y^2)} \times \sum_{s=1}^M \int \int_{-\infty}^{\infty} \left\{ \frac{e^{-j\frac{2\pi}{\lambda} z_f}}{j \lambda z_f} \mathcal{F}\{U_s(x, y) e^{-j\phi_s(x, y)}\} \right\} \left[\frac{-j z_f z_s}{\lambda z_f^2 |z_s - z_i|} \mathcal{F}\left\{ e^{-j\frac{\pi z_f z_s}{\lambda z_f^2} \frac{(x^2+y^2)}{|z_s - z_i|}} \right\} \right] e^{-j2\pi(xf_x + yf_y)} df_x df_y \quad (19)$$

$$W(x, y, z_i) = \frac{z_f}{z_i} e^{j\frac{2\pi}{\lambda}(z_i-z_f)} e^{j\frac{\pi}{\lambda z_i}(x^2+y^2)} U_f(x, y) e^{-j\phi_f(x, y)} + \frac{j}{\lambda} \sum_{s=1}^M \frac{z_s}{z_f |z_s - z_i|} e^{j\frac{2\pi}{\lambda}(z_i-z_f)} e^{j\frac{\pi}{\lambda z_i}(x^2+y^2)} \times \int \int_{-\infty}^{\infty} \mathcal{F}\{U_s(x, y) e^{-j\phi_s(x, y)}\} \mathcal{F}\left\{ e^{-j\frac{\pi z_f z_s}{\lambda z_f^2} \frac{(x^2+y^2)}{z_s - z_i}} \right\} e^{-j2\pi(xf_x + yf_y)} df_x df_y \quad (20)$$

Thus, each element of the second term is in the form of the inverse Fourier transform of the product of Fourier transforms of two functions. Using the convolution property, they can be replaced by the Fourier transform of their convolution, which cancels the inverse Fourier transform

$$W(x, y, z_i) = \frac{z_f}{z_i} e^{j\frac{2\pi}{\lambda}(z_i-z_f)} e^{j\frac{\pi}{\lambda z_i}(x^2+y^2)} U_f(x, y) e^{-j\phi_f(x, y)} + j \sum_{s=1}^M \frac{z_s}{\lambda z_f (z_s - z_i)} e^{j\frac{2\pi}{\lambda} z_i} e^{j\frac{\pi}{\lambda z_i}(x^2+y^2)} \left(U_s(x, y) e^{-j\phi_s(x, y)} \otimes e^{-j\frac{\pi z_f z_s}{\lambda z_f^2} \frac{(x^2+y^2)}{z_s - z_i}} \right) \quad (21)$$

Next, we simplify the notation by introducing $\alpha^2 = \frac{\lambda z_f^2}{\pi z_f z_s} (z_s - z_i)$, $k = \frac{z_f}{z_i} e^{j\frac{2\pi}{\lambda}(z_i-z_f)} e^{j\frac{\pi}{\lambda z_i}(x^2+y^2)}$ and $k' = \frac{z_s}{\lambda z_f |z_s - z_i|} e^{j\frac{2\pi}{\lambda}(z_i-z_f)} e^{j\frac{\pi}{\lambda z_i}(x^2+y^2)} = \frac{z_f z_s}{\lambda z_f^2 |z_s - z_i|} k$:

$$W(x, y, z_i) = k \frac{U_f(x, y) e^{-j\phi_f(x, y)}}{\text{Desired image} \text{Random phase}} + j \sum_{s=1}^M k' (U_s(x, y) e^{-j\phi_s(x, y)} \otimes e^{-j(\alpha^2+x^2+y^2)/\alpha^2}) \quad (22)$$

The series term contains the convolution of the product of the other images and their random phases with a parabolic phase (wavefront). The convolution with a parabolic phase plays a very important role, because it mixes the random phase with the amplitude, rendering both the amplitude and phase of the resulting field random. This effect is illustrated in Supplementary Fig. 9.

We want to compare the magnitude of the first term with the magnitudes of the terms within the series. Before we can do so, we should arrange for the integration due to the convolution to be over dimensionless coordinates. To achieve this, we transform the entire equation into normalized (dimensionless) lateral coordinates through the transformation $x \rightarrow \alpha x'$ and $y \rightarrow \alpha y'$. By its definition, the convolution term is

$$U_s(x, y) e^{-j\phi_s(x, y)} \otimes e^{-j(\alpha^2+x^2+y^2)/\alpha^2} = \int \int_{-\infty}^{\infty} U_s(x-u, y-v) e^{-j\phi_s(x-u, y-v)} e^{j\frac{(u^2+v^2)}{\alpha^2}} du dv \quad (23)$$

Introducing the normalized coordinates, $u = \alpha u'$, $v = \alpha v'$, $x = \alpha x'$ and $y = \alpha y'$

$$U_s(x, y) e^{-j\phi_s(x, y)} \otimes e^{-j(\alpha^2+x^2+y^2)/\alpha^2} = \alpha^2 \int \int_{-\infty}^{\infty} U_s(\alpha x' - \alpha u', \alpha y' - \alpha v') e^{-j\phi_s(\alpha x' - \alpha u', \alpha y' - \alpha v')} e^{j(u'^2+v'^2)} du' dv' \quad (24)$$

We now introduce the new functions $U'_i(x', y')$ and $\phi'_i(x', y')$, taking the normalized coordinates as their parameters, but otherwise identical in form, amplitude and unit, as $U_i(x, y)$ and $\phi_i(x, y)$. To give a concrete example, for $U_f(x, y) = U_0 e^{-(x+y)^2/\alpha^2}$ the new function would become $U'_f(x', y') = U_0 e^{-(x'+y')^2}$. The convolution takes the form

$$U_s(x, y) e^{-j\phi_s(x, y)} \otimes e^{-j(\alpha^2+x^2+y^2)/\alpha^2} = \alpha^2 \int \int_{-\infty}^{\infty} U'_s(x' - u', y' - v') e^{-j\phi'_s(x' - u', y' - v')} e^{j(u'^2+v'^2)} du' dv' = \alpha^2 U'_s(x', y') e^{-j\phi'_s(x', y')} \otimes e^{-j(x'^2+y'^2)} \quad (25)$$

Similarly, $W(x, y)$ gets mapped to $W'(x', y')$ and using the relation $\alpha^2 k' = k/\pi$ to simplify, $W'(x', y')$ is given by

$$W'(x', y', z_i) = k(U'_f(x', y') e^{-j\phi'_f(x', y')} + \frac{j}{\pi} \sum_{s=1}^M U'_s(x', y') e^{-j\phi'_s(x', y')} \otimes e^{-j(x'+y')^2}) \quad (26)$$

This expression can be analysed to clearly reveal how the random phase suppresses crosstalk. As mentioned at the beginning of this section, the 3D image formed on any conventional detector or an image viewed through a scattering process is given by $|W'(x', y', z_i)|^2$. To simplify further, we introduce $Y_s(x', y') \equiv U'_s(x', y') e^{j\phi'_s(x', y')} \otimes e^{j(x'^2+y'^2)}$. We note that all $Y_s(x', y')$ are random, because they are all convolutions of $U'_s(x', y')$ and $e^{j\phi'_s(x', y')}$ the product of the coherent amplitude defining the image, $U'_s(x', y')$ and the random phase corresponding to that image, $e^{j\phi'_s(x', y')}$, with a parabolic wavefront, $e^{-j(x'+y')^2}$. This operation is sufficient to thoroughly mix the non-random amplitude information defining the image with the random phase information. The end result is virtually completely random valued (Supplementary Fig. 9), except in the limiting case of $\alpha \rightarrow 0$, in which case $e^{-j(x'+y')^2} \rightarrow \delta(x', y')$ and the convolution operation yields $U'_s(x', y') e^{j\phi'_s(x', y')}$ unaltered. However, $\alpha \rightarrow 0$ implies $z_i \rightarrow z_s$, which would mean that the two images are already in the same plane. Thus, this limit is not relevant in practice.

Next, we calculate the value of $|W'(x', y', z_i)|^2$:

$$|W'(x', y', z_i)|^2 = |k|^2 (|U'_f(x', y')|^2 + \frac{1}{\pi^2} \sum_{s=1}^M |Y_s(x', y')|^2 + \frac{j}{\pi} \sum_{s=1}^M (U'_f(x', y')^* e^{j\phi'_f(x', y')} Y_s(x', y') - U'_f(x', y') e^{-j\phi'_f(x', y')} Y_s(x', y')^*) + \frac{1}{\pi^2} \sum_{s=1}^M \sum_{m=1}^M (Y_s(x', y')^* Y_m(x', y') + Y_s(x', y') Y_m(x', y')^*)) \quad (27)$$

We now discuss each of the terms of the result above. The first term, $|U'_f(x', y')|^2$, corresponds to the production of the desired image in perfect form, apart from an overall multiplicative constant, which is not important. The second term is a sum of $M-1$ random images, as discussed above. They are also mutually independent, so their summation is further closer to a constant value by the central limit theorem for large M . In practice, their role is to add a certain amount of white noise to the ideal image. Furthermore, their contribution is strongly suppressed by the prefactor of $\pi^2 \approx 10$, as well as the summation of $M-1$ of them. The third term is a sum over $M-1$ terms, each of which are in a form such that their contribution, averaged over the image (in all the examples considered here, N , the number of hologram pixels, varies between 10^5 and 10^7), is similar to inner products of very high dimensional (equivalent to N) mutually random vectors. Furthermore, unlike the second term, they do not involve absolute squares, so their random values are allowed to converge to zero. Together with the near-complete orthogonality of mutually random vectors in high dimensions, their contribution vanishes in the limit of large dimensions, that is, a large number of pixels in the images and a large number of planes. The fourth term involves in the order of M^2 terms, which vanish for the same reasons, but even faster due to their large numbers for large M .

Overall, we see that the final result for any image plane, i , is that we obtain the ideal image, $|U_f(x, y)|^2$, only with the addition of some amount of white noise. There remains absolutely no trace of any coherent manifestation of any of the other images. We declare crosstalk to have been suppressed (see Supplementary Fig. 10 for a simple demonstration for the case of $M=2$). Finally, we note that the demonstrations here were restricted to the use of pure phase holograms, $F_i(x, y)$, for practical reasons. This limitation causes additional deterioration of the image

reproduction, which can be avoided at the cost of increased complexity of the experimental implementation, if so desired.

Data availability

The data that support the plots within this paper and other findings of this study are available from the corresponding authors upon reasonable request.

References

39. Gorban, A. N. & Tyukin, I. Y. Blessing of dimensionality: mathematical foundations of the statistical physics of data. *Philos. Trans. A Math. Phys. Eng. Sci.* **376**, 20170237 (2018).
40. Révész, P. *The Laws of Large Numbers* (Academic Press, 1967).